

# Hadamard Slice Encoding for Reduced-FOV Diffusion-Weighted Imaging

Emine Ulku Saritas,<sup>1,2,3\*</sup> Daeho Lee,<sup>1</sup> Tolga Çukur,<sup>1,2,3</sup> Ajit Shankaranarayanan,<sup>4</sup> and Dwight G. Nishimura<sup>1</sup>

**Purpose:** To improve the clinical utility of diffusion-weighted imaging (DWI) by extending the slice coverage of a high-resolution reduced field-of-view technique.

**Theory:** Challenges in achieving high spatial resolution restrict the use of DWI in assessment of small structures such as the spinal cord. A reduced field-of-view method with 2D echo-planar radiofrequency (RF) excitation was recently proposed for high-resolution DWI. Here, a Hadamard slice-encoding scheme is proposed to double the slice coverage by exploiting the periodicity of the 2D echo-planar RF excitation profile.

**Methods:** A 2D echo-planar RF pulse and matching multiband refocusing RF pulses were designed using the Shinnar-Le Roux algorithm to reduce band interference, and variable-rate selective excitation to shorten the pulse durations. Hadamard-encoded images were resolved through a phase-preserving image reconstruction. The performance of the method was evaluated via simulations, phantom experiments, and in vivo high-resolution axial DWI of spinal cord.

**Results:** The proposed scheme successfully extends the slice coverage, while preserving the sharp excitation profile and the reliable fat suppression of the original method. For in vivo axial DWI of the spinal cord, an in-plane resolution of  $0.7 \times 0.7 \text{ mm}^2$  was achieved with 16 slices.

**Conclusion:** The proposed Hadamard slice-encoding scheme doubles the slice coverage of the 2D echo-planar RF reduced field-of-view method without any scan-time penalty. **Magn Reson Med 72:1277–1290, 2014.** © 2013 Wiley Periodicals, Inc.

**Key words:** diffusion-weighted imaging; Hadamard encoding; multiband excitation; reduced field-of-view; 2D RF pulse

## INTRODUCTION

High in-plane resolution is essential for diffusion-weighted imaging (DWI) of small structures, such as the spinal cord. However, the performance of conventional DWI methods can be hindered by a variety of sources

including susceptibility variations, field inhomogeneities and bulk physiologic motion. Although multishot techniques offer high resolution, they are also sensitive to motion-induced phase errors during diffusion-encoding gradients (1). These phase errors are unpredictable and different for each shot, and can result in ghosting artifacts and overestimated apparent diffusion coefficients (ADC). Single-shot echo-planar imaging (ss-EPI), on the other hand, is robust to motion, as it acquires the entire k-space in one shot. Due to its relatively long readouts, however, ss-EPI suffers from blurring in the phase-encode (PE) direction and significant distortions and/or artifacts due to off-resonance (e.g., from susceptibility differences among various types of tissues,  $B_0$ -inhomogeneities, chemical shift between fat/water, etc.).

Recently, a number of reduced field-of-view (FOV) methods have been proposed for high-resolution DWI of small structures (2–7). In general, these methods reduce the FOV in the PE direction ( $FOV_{PE}$ ) to only cover the region of interest (ROI). This in turn decreases the number of required k-space lines for a given image resolution, reducing off-resonance induced artifacts in ss-EPI images. Most reduced-FOV methods use additional/supplementary radiofrequency (RF) pulses to suppress the signal from tissues outside the ROI. One such method called ZOOM-EPI (2) combines a regular  $90^\circ$  excitation pulse with an obliquely applied  $180^\circ$  refocusing pulse to obtain a reduced FOV. However, due to its parallelogram-shaped inner volume, adjacent slices suffer from signal drop along the edges of the ROI. Hence, this method requires a slice skip between adjacent slices or an extended  $FOV_{PE}$  to alleviate the signal loss. Alternatively, one can utilize outer-volume suppression pulses to reduce the FOV (3). If the suppression is not 100% effective, there may be partial aliasing artifacts along the PE direction of the image. Another technique applies excitation and refocusing RF pulses orthogonally (4), which decreases the signal-to-noise ratio (SNR) of the neighboring slices. A double spin-echo method was proposed to alleviate this issue (7); however, its performance can be compromised by  $B_1$  field inhomogeneities and the prolonged echo times (TE).

A fundamentally different approach to reduced-FOV imaging is to actively excite only the ROI by using a 2D echo-planar RF (2D-EPRF) excitation pulse (5). This method achieves a sharp excitation profile in the PE direction, enables contiguous multislice imaging without the need for a slice skip, and suppresses the fat signal. Because the outer volume is never excited, there is no aliasing along the reduced-FOV direction. This method was previously evaluated in a clinical setting, and was shown not only to be superior to standard full-FOV DWI

<sup>1</sup>Department of Electrical Engineering, Stanford University, Stanford, California, USA.

<sup>2</sup>Department of Electrical and Electronics Engineering, Bilkent University, Bilkent, Ankara, Turkey.

<sup>3</sup>National Magnetic Resonance Research Center (UMRAM), Bilkent University, Bilkent, Ankara, Turkey.

<sup>4</sup>Global Applied Science Laboratory, GE Healthcare, Menlo Park, California, USA.

\*Correspondence to: Emine U. Saritas, Ph.D., Department of Electrical and Electronics Engineering, Bilkent University, Bilkent, Ankara 06800, Turkey. E-mail: saritas@ee.bilkent.edu.tr

Received 10 July 2013; revised 22 October 2013; accepted 24 October 2013

DOI 10.1002/mrm.25044

Published online 21 November 2013 in Wiley Online Library (wileyonlinelibrary.com).

methods (8) but also to increase the confidence in the diagnosis of common spinal pathologies (9). However, due to the periodicity of the 2D excitation profile along the slice direction, only a certain number of slices can be imaged simultaneously without affecting the signal level. For certain applications where the ROI is relatively small in the slice direction, this limit is not of concern. For example, sagittal imaging of the spinal cord requires only 1–2 cm coverage in slice direction, which can easily be achieved with 3–5 slices of 4-mm thickness. In contrast, for other applications such as the axial imaging of the spinal cord, it is desirable to acquire as many slices as possible along the length of the spine, to avoid multiple acquisitions and long scan times. One proposed solution to this problem is to swap the slice and slab directions of the 2D-EPRF pulse, so that the periodicity is along the slab direction (6). This approach alleviates the limit on the number of slices. However, because the slab direction is also the PE direction during imaging, the periodicity may now cause aliasing along the PE direction of the acquired images. To avoid this problem, one needs to sacrifice the sharpness of the excitation profile. The resulting wide transition bands require prescribing an extended FOV<sub>PE</sub>, similar to the ZOOM-EPI method. Moreover, the fat suppression capability of the 2D-EPRF method is compromised, and additional fat suppression pulses are needed.

In this work, we propose a Hadamard slice-encoding scheme (10–13) to increase the slice coverage of the 2D-EPRF method. This Hadamard scheme exploits the periodicity of the 2D-EPRF excitation profile, while maintaining the sharp excitation profiles in the PE direction and the inherent fat suppression capability. In contrast to previously proposed multiband methods that simultaneously excite multiple slices/slabs (10–13), we perform “multiband refocusing” by applying a Hadamard scheme on the 180° refocusing RF pulse of the spin-echo ss-EPI imaging sequence. We use the Shinnar-Le Roux (SLR) RF pulse design algorithm to reduce band interference (13–16), and variable-rate selective excitation (VERSE) to shorten the pulse durations (17–19). We validate the performance of the method with phantom experiments and in vivo high-resolution axial DWI of the spinal cord. In addition, we evaluate its sensitivity to timing errors, off-resonance, and  $B_1$  field inhomogeneities using Bloch simulations. We show that the proposed Hadamard slice-encoding scheme can successfully double the slice coverage for the reduced-FOV method, without any scan-time penalty.

## THEORY

The 2D-EPRF pulse we utilize for reduced-FOV imaging provides independent control over the slice and slab thicknesses, and can achieve a high aspect ratio between the two thicknesses. Figure 1a shows the periodic 2D excitation profile for a 2D-EPRF pulse. Here, the slab direction corresponds to the PE direction during imaging, and the limited extent of excitation in that direction enables efficient inner-FOV imaging. Due to the long RF pulse duration (typically longer than 15 ms), the excitation profile for fat is spatially shifted in the slice-select (SS) direction by

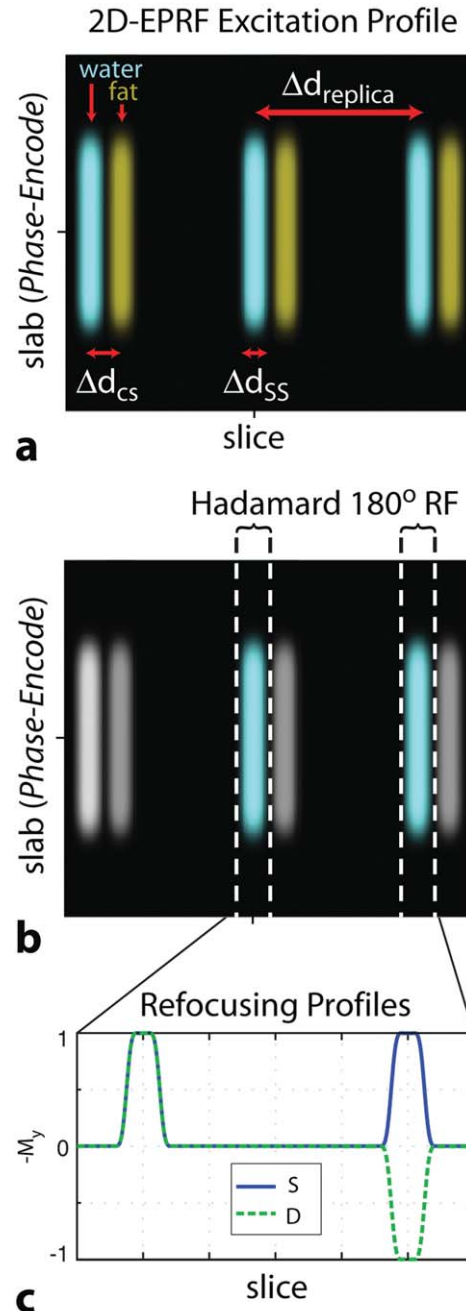


FIG. 1. The 2D-EPRF excitation profile and Hadamard multiband refocusing scheme. a: Simulated excitation profile for the 2D-EPRF pulse. The 2D profile is periodic in the slice direction, with nonoverlapping fat and water profiles (shown in green and blue, respectively). Here, only three lobes are displayed for water and fat profiles, but the periodicity extends on both sides in the slice direction. The slab direction corresponds to the phase-encode (PE) direction during imaging. The limited extent of excitation in the PE direction enables reduced-FOV imaging. b: A Hadamard 180° RF pulse can be used to acquire multiple lobes at once. This RF pulse acts on two adjacent lobes of the 2D excitation water profile. While these two lobes are refocused, the signal from fat and the remaining lobes are all suppressed. c: For the Hadamard encoding scheme, two separate Hadamard 180° RF pulses are designed. The first RF pulse refocuses both lobes with the same phase (S), and the second one with opposite phase (D). By combining images from these two cases, we can resolve both lobes.

$$\Delta d_{cs} = f_{cs} \frac{\Delta d_{SS} N_{\text{blip}} T_{\text{fast}}}{TBW_{SS}}, \quad [1]$$

where  $f_{cs}$  is the chemical shift,  $\Delta d_{SS}$  is the slice thickness,  $T_{\text{fast}}$  is the duration between two consecutive gradient blips,  $N_{\text{blip}}$  and  $TBW_{SS}$  are the number of gradient blips and the time-bandwidth product (TBW) of the RF pulse in the SS-direction, respectively. We can exploit this spatial shift to suppress the fat signal. First, we carefully choose the 2D-EPRF pulse parameters to generate nonoverlapping fat and water profiles (i.e.,  $\Delta d_{cs} > \Delta d_{SS}$ ). Next, we apply a subsequent  $180^\circ$  RF pulse with crushers to refocus the water signal while suppressing fat. Further details on this excitation/suppression scheme can be found in Ref. (5).

One important feature of this reduced-FOV method is its contiguous multislice imaging capability. Because the adjacent slices are not excited, multiple slices can be collected in an interleaved fashion in a single repetition time (TR) without affecting the signal level. However, because the blipped gradients discretely sample the excitation k-space, the excitation profile is periodic in the SS-direction (see Figure 1a). Depending on the TR, the replicas of the main lobe may not have fully recovered by the time that location is imaged. This partial saturation of sidelobe locations can diminish the SNR. Hence, the periodicity of the profile places a limit on the number of slices that can be acquired without affecting the signal level:

$$N_{\text{slice}} = \frac{\Delta d_{\text{replica}}}{\Delta d_{SS}} = \frac{N_{\text{blip}}}{TBW_{SS}}. \quad [2]$$

This limit is equal to the number of slices that can fit between two adjacent lobes, where  $\Delta d_{\text{replica}}$  is the interlobe distance. There is a clear trade-off between the pulse duration (made longer by large  $N_{\text{blip}}$  values) and  $N_{\text{slice}}$ . Furthermore, smaller slab thicknesses (i.e., smaller  $\text{FOV}_{\text{PE}}$ ) require even longer RF pulse durations to achieve a given  $N_{\text{slice}}$ . To avoid long TE, RF amplifier heating, and profile distortions due to relaxation, we limit the 2D-EPRF pulse duration to a maximum of 20 ms. To maximize the efficiency of the pulse, we utilize a variable-rate selective excitation (VERSE) algorithm, such that the ramp up/down portions of the trapezoidal gradients are also used for RF excitation. As a result, we achieve  $N_{\text{slice}} = 8$  and  $\text{FOV}_{\text{PE}} = 4$  cm with a 19.8 ms 2D-EPRF pulse (see Figure 1a).

To increase the number of slices, we exploit the periodic nature of the 2D-EPRF profile. We design  $180^\circ$  RF pulses that refocus two adjacent lobes to generate the following summation ( $S$ ) and difference ( $D$ ) images:

$$S = \text{Slice}_k + \text{Slice}_{N+k} \quad [3a]$$

$$D = \text{Slice}_k - \text{Slice}_{N+k}, \quad [3b]$$

where  $N$  is same as  $N_{\text{slices}}$ . The original slices can then be resolved by combining these two images:

$$\text{Slice}_k = (S + D)/2 \quad [4a]$$

$$\text{Slice}_{N+k} = (S - D)/2. \quad [4b]$$

Performing this in all original slice locations doubles the number of resolved slices. In DWI, it is customary to acquire multiple averages to attain sufficient signal levels. If

NEX is the number of averages in the original imaging scheme, here we propose acquiring NEX/2 averages for  $S$  and NEX/2 averages for  $D$ , so that the slice coverage is doubled without changing the total scan time. Note that the signal from each slice is acquired during both  $S$  and  $D$ , so the effective number of averages per slice is still equal to NEX. Hence, in theory, the doubling of the slice coverage comes without any SNR penalty.

To generate  $S$  and  $D$  images, we need two separate  $180^\circ$  RF pulses: One that generates the same phase, and one that generates  $180^\circ$  phase offset on the two adjacent lobes. This Hadamard RF pulse pair (denoted as  $RF_S$  and  $RF_D$ ) is designed using the SLR design algorithm (13,16), which provides more accurate profiles and reduces band interference when compared to the conventional method of summing the RF pulses for each band. Once the Hadamard pulses are designed, we utilize a time-optimal VERSE algorithm to shorten their durations. These steps are summarized in Figure 2 and explained in detail in the following sections.

### Pulse Design with SLR Transform

Hadamard RF pulses generate more accurate profiles and reduced band interference when designed using the SLR transform, instead of the conventional method of summing the RF pulses for each band (13). This is particularly important in our case, because the bands can be spatially close and the tip angle is large for the  $180^\circ$  RF pulses. A detailed explanation of the use of the SLR transform for designing Hadamard excitation pulses is given in (13). Here, we describe the application of the SLR transform for designing Hadamard refocusing RF pulses.

The SLR transform maps a sampled RF waveform,  $B_1(t)$ , to two polynomials,  $A_n(z)$  and  $B_n(z)$ :

$$B_1(t) \xleftrightarrow{\text{SLR}} (A_n(z), B_n(z)), A_n(z) = \sum_{j=0}^{n-1} a_j z^{-j}, B_n(z) = \sum_{j=0}^{n-1} b_j z^{-j}. \quad [5]$$

Here,  $n$  is the number of RF pulse samples,  $a_j$  and  $b_j$  are polynomial coefficients,  $z$  is a phasor defined as  $z = e^{i\gamma G x \Delta t}$ , where  $\gamma$  is the gyromagnetic ratio,  $G$  is the gradient strength,  $x$  is the spatial coordinate, and  $\Delta t$  is the sampling interval.

For the Hadamard RF pulses, we start by designing the  $B_n(z)$  polynomial for a single-band refocusing pulse using the least-squares digital-filter-design algorithm. The coefficients of this polynomial are then modulated and combined to produce composite  $B_n(z)$  polynomials:

$$b_{j,S} = b_j \cdot (e^{iw(j-(1-\beta)n)\Delta t} + e^{-iw(j-(1-\beta)n)\Delta t}) \quad [6a]$$

$$b_{j,D} = b_j \cdot (e^{iw(j-(1-\beta)n)\Delta t} + ie^{-iw(j-(1-\beta)n)\Delta t}) \quad [6b]$$

where  $\pm w$  is given by

$$w = \gamma G \frac{\Delta d_{\text{replica}}}{2}. \quad [7]$$

In these expressions,  $b_{j,S}$  and  $b_{j,D}$  are the coefficients of  $B_n(z)$  for the two Hadamard pulses  $RF_S$  and  $RF_D$ ,

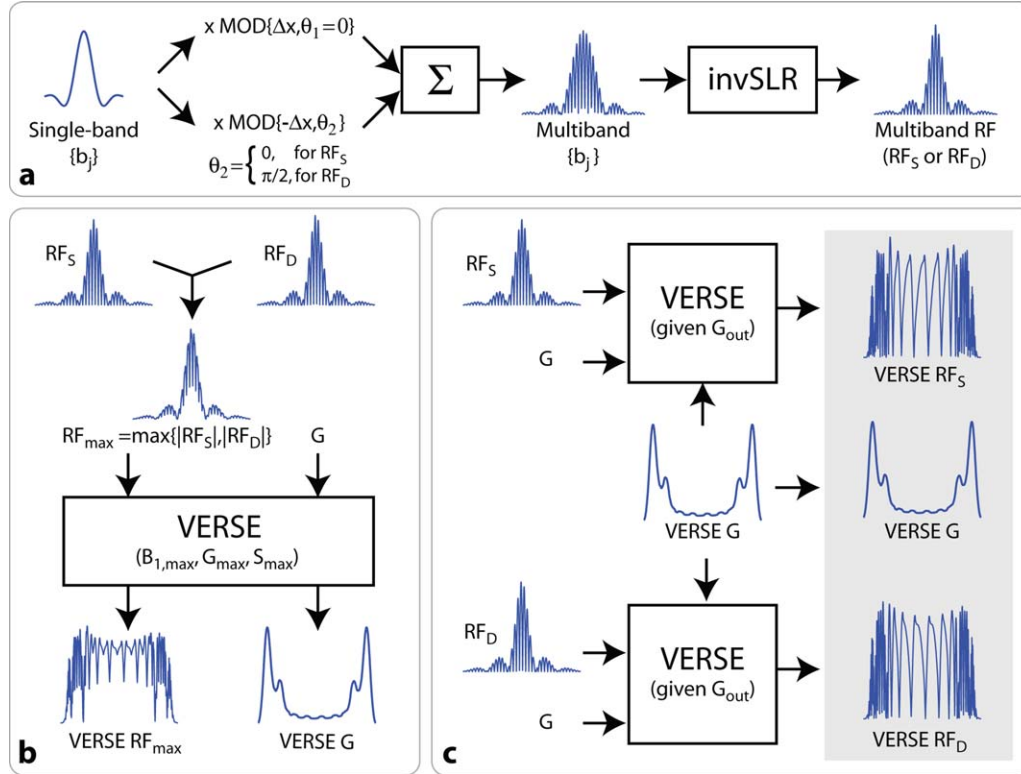


FIG. 2. Flow chart describing the Hadamard  $180^\circ$  RF pulse design: **a**: The  $B_n(z)$  polynomial coefficients,  $\{b_j\}$ , of a regular single-band RF pulse are modulated by complex exponentials and summed. Inverse SLR (invSLR) transform is then applied to the resulting multiband  $\{b_j\}$  to obtain a Hadamard RF pulse (either  $RF_S$  or  $RF_D$ ).  $\Delta x$  and  $\theta_i$  denote the spatial shift and phase for each band, respectively. This step is individually performed for both the  $RF_S$  and  $RF_D$  pulses with one difference: the second band has  $\theta_2 = 0$  for  $RF_S$  and  $\theta_2 = \pi/2$  for  $RF_D$  (see Eq. [6]). **b**: The point-by-point maximum of the  $RF_S$  and  $RF_D$  pulses (denoted as  $RF_{\max}$ ) and the corresponding constant gradient  $G$  are VERSEd to get the shortest RF/gradient pair for given hardware limits. **c**: Using the VERSE algorithm,  $RF_S$  and  $RF_D$  pulses are individually reshaped to match the time-varying VERSE  $G$  calculated in the previous step. The resulting pulses are VERSE  $\{RF_S, RF_D\}$ , with both pulses using the same SS gradient waveform VERSE  $G$ . [Color figure can be viewed in the online issue, which is available at [wileyonlinelibrary.com](http://wileyonlinelibrary.com).]

respectively. The corresponding RF pulses will refocus two lobes that are spaced apart by  $\Delta d_{\text{replica}}$ , as shown in Figure 1b,c. The parameter  $\beta$  denotes the location of the effective temporal center for the single-band RF pulse, and is equal to 0.5 for the RF pulses presented in this work, as the effective center coincides with the temporal midpoint (13). Note that the second exponential term on the right hand side of Eq. [6b] is multiplied by  $i$ , and not  $-1$  as done for Hadamard excitation pulses. Multiplying by  $-1$  would cause a  $-180^\circ$  rotation for that band, which is equivalent to a  $+180^\circ$  rotation. Multiplying by  $i$ , on the other hand, changes the axis of rotation by  $90^\circ$ , so that the refocused spins in that band will have inverted polarity, as desired.

Once the  $B_n(z)$  coefficients are calculated,  $A_n(z)$  is derived through a Hilbert transform relation (16). Finally, the inverse SLR transform is utilized to obtain the Hadamard RF pulses,  $RF_S$  and  $RF_D$ .

#### Pulse Reshaping by VERSE

The Hadamard  $180^\circ$  pulses are in effect complex combinations of two single-band  $180^\circ$  RF pulses. Therefore, these pulses can result in twice the peak  $B_1$  amplitude of

their single-band counterparts, which can easily exceed hardware limitations for maximum  $B_1$  field. If we instead keep the peak  $B_1$  constant (a more practical solution), Hadamard pulses will be twice as long in duration. These long RF pulses (e.g., 15 ms) are undesirable, as they lengthen the TE and distort the profile due to increased off-resonance and relaxation effects. In particular, an SNR loss can occur when these long pulses are used in conjunction with the already long 2D-EPRF pulse. Because the 2D-EPRF pulse durations are already minimized by utilizing the ramp up/down portions of the trapezoidal gradient waveforms, we need to shorten the Hadamard pulses instead.

To avoid SNR losses, we propose shortening the Hadamard pulse durations using a time-optimal variable-rate selective excitation (VERSE) algorithm that jointly reshapes  $\{RF_S, RF_D\}$ . By exploiting the VERSE principle, we jointly reshape the RF/gradient waveforms without changing the on-resonant excitation profile (17–19). Specifically, VERSE can be used to compute the shortest waveform pair for a given peak RF amplitude within specified hardware limits (e.g., maximum gradient and slew rate). The time-efficiency stems from the systematic and localized reshaping of the high power regions of RF

waveforms. Using VERSE, RF amplitude can be lowered by proportionally reducing the corresponding gradient amplitude in excitation k-space (19). The particular VERSE algorithm used in this work is called “time-optimal VERSE” (19), which provides a noniterative time-optimal solution.

During the pulse reshaping process, we must avoid any discrepancies between the  $\{RF_S, RF_D\}$  pulses that could result in crosstalk between the resolved slices. For example, any difference in TE between the  $S$  and  $D$  images would result in a disparity between the signal levels, or the use of different SS gradient amplitudes would yield slightly different effective  $b$ -values due to gradient crosstalk (20). We can avoid this issue by sharing the same gradient waveform, time-efficiently designed, for both RF waveforms.

As illustrated in Figure 2b, we start by computing a composite pulse,  $RF_{\max}$ , by taking the maximum amplitude of the two RF pulses at each instant:

$$RF_{\max}(t) = \max\{|RF_S(t)|, |RF_D(t)|\}. \quad [8]$$

Next, the time-optimal VERSE method is applied to the composite pulse pair  $\{RF_{\max}, G\}$  to calculate the shortest gradient waveform, VERSE  $G$ , within the hardware limits. As shown in Figure 2c,  $RF_S$  and  $RF_D$  are then individually reshaped to match this time-varying VERSE  $G$ . During this reshaping process, we exploit the constant RF-to-gradient relationship of VERSE principle (19). Finally, we arrive at the desired Hadamard pulse pairs, VERSE  $\{RF_S, G\}$  and VERSE  $\{RF_D, G\}$ . Note that using  $RF_{\max}$  during the time-optimal VERSE design guarantees that the resulting VERSE  $\{RF_S, RF_D\}$  pulses conform to all hardware limits, while sharing the shortest-duration gradient waveform, VERSE  $G$ .

## METHODS

To test the performance of the proposed Hadamard slice-encoding method, a 2D-EPRF pulse and matching Hadamard  $180^\circ$  RF pulses were designed. For the imaging experiments described in this section, we used the VERSE versions of the Hadamard RF pulses. The SLR transform, time-optimal VERSE and Bloch equation simulations were implemented in MATLAB (The Mathworks Inc., Natick, MA). Phantom experiments and in vivo imaging were performed on a 1.5 T GE Excite scanner (40 mT/m maximum gradient strength and 150 mT/m/ms maximum slew rate).

### RF Pulses and Simulations

The 2D-EPRF pulse was designed using the following parameters:  $N_{\text{slice}} = 8$ , 5-mm slice thickness,  $\Delta d_{\text{replica}} = 40\text{mm}$ , 4.5-cm slab thickness (i.e., reduced-FOV) in PE direction,  $TBW_{\text{SS}} = 3$ ,  $TBW_{\text{PE}} = 10$ , peak  $B_1 = 15\ \mu\text{T}$ , 19.8 ms total RF pulse duration. The resulting excitation profile is shown in Figure 1a. For time efficiency, the 2D-EPRF pulse was designed such that the RF power is deposited during both the ramps and plateaus of the echo-planar gradients. The blipped gradients were placed at the end of every other RF sublobe,

i.e., each excitation k-space line was traversed forward and back. The resultant excitation k-space trajectory is a hybrid between regular and fly-back echo-planar trajectories, and prevents the so-called “ghost” excitations that would otherwise appear halfway between the periodic sidelobes in the case of a delay between RF and gradient waveforms.

Next, the Hadamard  $180^\circ$  RF pulses that match the 2D excitation profile were designed following the steps in Figure 2a. The initial single-band RF pulse had  $TBW = 5$ , in- and out-of-slice ripples of 0.1%, number of samples = 500, and  $\beta = 0.5$ . The duration of this RF pulse was 7.8 ms for a peak  $B_1$  amplitude of  $15\ \mu\text{T}$ . The  $B_n(z)$  polynomial coefficients for this pulse were modulated and summed as in Eq. [6]. During the modulation process,  $\Delta d_{\text{replica}}/2 = 20\text{mm}$  was utilized. Taking the inverse SLR transform of the resulting multiband polynomials produced the initial Hadamard RF pulses, which were stretched in time to meet the peak  $B_1$  requirement of  $15\ \mu\text{T}$ . For both  $RF_S$  and  $RF_D$ , the resulting pulse durations were 15.5 ms, with a gradient amplitude of  $G = 1.4\text{mT/m}$  for 5-mm slice thickness.

The sample-wise maximum of the  $|RF_S|$  and  $|RF_D|$  pulses,  $RF_{\max}$ , was then computed.  $RF_{\max}$  and the corresponding  $G = 1.4\text{mT/m}$  were then run through a VERSE algorithm to generate the time-optimal pulses within the following hardware limits:  $B_{1,\max} = 15\ \mu\text{T}$ ,  $G_{\max} = 40\text{mT/m}$ ,  $S_{\max} = 150\text{mT/m/ms}$ . To avoid gradient waveform distortions due to eddy currents or amplifier bandwidth limits (18), the VERSE  $G$  waveform was smoothed with a moving average window of  $164\ \mu\text{s}$ . Finally, the  $RF_S$  and  $RF_D$  pulses were individually reshaped to match the VERSE  $G$  waveform. The resulting VERSE  $\{RF_S, RF_D, G\}$  pulses were 3.6 ms in duration.

Power depositions of RF pulses were compared via calculating the integral of the squared RF amplitudes, i.e.,  $\int |B_1(t)|^2 dt$ . We also performed Bloch simulations to evaluate the slice profiles for the resulting VERSE  $\{RF_S, RF_D\}$  pulses. The sensitivity of the VERSE pulses to timing delays between RF and gradient waveforms was assessed for a delay range of  $-16$  to  $16\ \mu\text{s}$ . RF/gradient delays cause increased levels of crosstalk between the resolved slices. To quantitatively analyze the crosstalk level, we integrated the crosstalk signal and normalized by the integrated signal from the original slice.

Depending on the size of the FOV, the global field inhomogeneity around the cervical spinal cord can be as high as 6 ppm (21). This is mostly due to abundance of air/tissue interfaces near the spine, and is especially important for sagittal/coronal imaging of the spine where larger FOVs are usually prescribed. The imaging volumes in our in vivo experiments were relatively small, thanks to the reduced-FOV imaging, which helps reduce the extent of field offsets. In addition, local first- and second-order shimming of the cord can alleviate a big portion of the field inhomogeneity problems. However, susceptibility variations between various tissues (e.g., vertebrae, muscle, CSF, gray/white matter) can induce approximately 0.5 ppm local off-resonances on the cord (22), which is harder to fix via shimming the ROI. Hence, the robustness against off-resonance was investigated by repeating the profile simulations for resonant

offsets of up to 64 Hz, corresponding to 1 ppm off-resonance at 1.5 T. To compute the overall signal loss for each resolved slice, we integrated over the slice thickness and normalized by the on-resonant signal level. We also computed the effects of resonant offsets on interslice crosstalk. A similar analysis was performed to evaluate robustness against  $B_1$  field inhomogeneities.

### Phantom Experiments

To verify the refocusing slice profiles for the Hadamard  $180^\circ$  RF pulses, a custom-made rectangular phantom filled with 1% copper sulfate ( $\text{CuSO}_4$ ) doped water was imaged using a standard quadrature transmit/receive head coil. The dimensions of the phantom were  $14 \times 11 \times 4 \text{ cm}^3$ . This phantom lacked any inner structure, providing a flat magnetization profile that makes it ideal for measuring slice and/or refocusing profiles. To image the profiles, the  $180^\circ$  RF pulse of a regular spin-echo sequence was replaced with a Hadamard RF pulse (i.e., either VERSE  $RF_S$  or VERSE  $RF_D$ , both with 3.6 ms duration), and the phase encoding was performed in the SS direction to resolve the slice profiles. The in-plane resolution was  $0.7 \times 0.7 \text{ mm}^2$ , with  $\text{TR} = 2000 \text{ ms}$  and  $\text{TE} = 24 \text{ ms}$ . To ensure an accurate measurement of the refocusing profiles, the 2D excitation pulse was made nonselective in the slice direction by setting the SS gradient waveform amplitude to zero. The slice thickness for the Hadamard  $180^\circ$  RF pulses were kept at 5 mm. Each acquisition was repeated 10 times to reduce the image noise. The data were averaged and zero padded by a factor of two. Finally, the central cross cuts of the images were chosen to represent the Hadamard slice profiles, and the resulting resolved slices were computed.

After measuring the slice profiles, the Hadamard pulses were incorporated into the reduced-FOV sequence to test their performance in conjunction with the 2D-EPRF pulse. For this experiment, a cylindrical resolution phantom (General Electric DQA phantom, Model 2131027-2,  $\text{NiCl}_2$ -doped water) was utilized. This phantom had various geometric features to help us evaluate whether there is any crosstalk between the resolved slices. Imaging was performed with a spin-echo 2DFT readout,  $\text{TR} = 2000 \text{ ms}$  with 8 interleaved excitations, and  $\text{TE} = 24 \text{ ms}$ . The FOV was  $9 \times 4.5 \text{ cm}^2$ , with  $\text{FOV}_{\text{PE}} = 4.5 \text{ cm}$  corresponding to the reduced-FOV direction (i.e., the slab direction of the 2D-EPRF pulse). Other imaging parameters were 5-mm slice thickness, no slice spacing,  $0.7 \times 0.7 \text{ mm}^2$  in-plane resolution,  $128 \times 64$  imaging matrix, 16 resolved slices (i.e.,  $N_{\text{slice}} = 8$  for the 2D-EPRF pulse, doubled due to the Hadamard encoding), and a total scan time of 4 min 16 s.

### In Vivo Imaging

In vivo imaging was conducted under the Institutional Review Board approval of GE Healthcare. To demonstrate the performance of the proposed method in vivo, axial DWI of the cervical spinal cord of a healthy subject was acquired using an 8-channel cervico-thoracic-lumbar (CTL) coil. 16 slices were resolved by applying the Hadamard slice-encoding scheme on the aforementioned 2D-EPRF pulse that had  $N_{\text{slice}} = 8$ . Following the 2D-EPRF excitation and Hadamard refocusing RF pulse, a spin-echo single-shot EPI

readout was used. Because the Hadamard scheme preserves the inherent fat suppression capability of the 2D-EPRF methods, no additional fat suppression pulses were needed. To improve robustness against pulsatile cord and CSF motion, the sequence was cardiac gated using the plethysmographic signal from a finger pulse oximeter, with two excitations per cycle and a 4-cardiac-cycle TR. Hence, a total of eight excitations were interleaved during each TR, with each excitation simultaneously acquiring two slice locations due to Hadamard encoding. To ensure minimum bulk motion during the diffusion sensitizing gradients, a 400 ms delay was used following peak systole (23). The total scan time varied from 4 to 5 min, depending on the heart rate. In the axial imaging plane, the readout direction was chosen as the anterior-posterior (A/P) direction, and the PE direction was the right-left (R/L) direction. The imaging FOV was  $9 \times 4.5 \text{ cm}^2$  FOV. Here,  $\text{FOV}_{\text{PE}} = 4.5 \text{ cm}$  corresponded to the reduced-FOV direction, i.e., the slab direction of the 2D-EPRF pulse. Other imaging parameters were  $0.7 \times 0.7 \text{ mm}^2$  in-plane resolution,  $128 \times 64$  imaging matrix, 62.5% partial k-space coverage in the PE direction (i.e., 40 PE lines in EPI readout), 5-mm slice thickness, no slice spacing,  $\text{TE} = 63 \text{ ms}$ .

Stejskal-Tanner spin-echo diffusion-weighting gradients (24) were applied in the superior-inferior (S/I), A/P, and R/L directions. A total of  $\text{NEX} = 20$  averages were acquired for all three directions, as well as for the  $T_2W$  image (i.e.,  $b = 0$ ). Half of the NEXs were spent acquiring  $S$  and the other half for  $D$ . The  $b$ -value was  $500 \text{ s/mm}^2$  for all directions. Note that for DWI of the spinal cord, typically lower  $b$ -values are utilized than in DWI of the brain, mainly due to the high diffusivity along the S/I direction of the cord. Values cited in the literature mostly range between 300 and  $700 \text{ s/mm}^2$  (25–29). Especially for high-resolution diffusion-weighted images, using high  $b$ -values would cause SNR-starved images when the diffusion weighting is along the S/I direction of the spine, which in turn would yield inaccurate ADC estimates. Based on the expected SNR of the images, one can approximate an optimal  $b$ -value to yield more accurate ADC estimates while keeping the SNR of the diffusion-weighted images above a certain threshold (30). For the imaging parameters that we used, we calculated that the optimal  $b$ -value is in the  $500 \text{ s/mm}^2$  range.

### Interleaved Averaging

Substantial crosstalk between resolved slices may occur if  $S$  and  $D$  images are misaligned due to involuntary motion of the subject. This problem can further be exacerbated as the temporal spacing between  $S$  and  $D$  may be prolonged with multiple averages (i.e., NEXs), increasing the probability of misalignment due to bulk motion. Therefore, to avoid cumulative motion artifacts in the resolved slices, the NEXs for  $S$  and  $D$  were acquired in an interleaved fashion (i.e., in two adjacent TRs). This interleaved averaging ensures that both images are similarly affected by motion, such that the resolved slices experience minimal levels of crosstalk.

### Image Reconstruction

For the phantom experiments, the individual slices were resolved by combining the Hadamard-encoded  $S$  and  $D$

images, as described in Eq. [4]. This simple reconstruction works reliably in the case of a phantom, or for the  $T_2$ -weighted in vivo images. However, the diffusion-weighted in vivo images may suffer from motion-induced dephasing and/or signal loss (1). Preserving both the phase and the amplitude of  $S$  and  $D$  is critical to avoid interference between the resolved slices. For example,  $S - D$  is not the same as  $|S| - |D|$ . To address these phase-related issues, we implemented the following reconstruction scheme for the diffusion-weighted in vivo images:

1. The individual images for  $S$  were phase corrected using a refocusing reconstruction (31). During this method, the central 12.5% of k-space data from each single-shot diffusion-weighted image was used as the “navigator data” for phase correction. The phase-corrected single-shot images were then complex averaged over all the repetitions. This procedure yields a combined image that is accurate in signal magnitude (i.e., does not suffer from signal loss that could result from combining dephased images).
2. A second image for  $S$  was reconstructed by direct complex averaging over all the repetitions. Due to potential differences between phases of individual single-shot images, this combined image may suffer from signal loss. Here, we assume that the motion-induced phase is made up of two components: (a) a reproducible phase term that is the same between all repetitions of an image [e.g., due to each repetition being acquired at the same time point in the cardiac cycle (32,33)], and (b) a phase noise that is random and uncorrelated between shots (e.g., due to involuntary subject motion). Direct averaging of such phase will retain the reproducible phase portion, whereas the random phase noise will average to zero given a sufficient number of repetitions are acquired.
3. The magnitude of the image from step 1 was combined with the phase of the image from step 2 to form a composite  $S$  image, that is,  $S_{\text{composite}} = |S_1|e^{i\angle S_2}$ . This composite image had accurate signal magnitude and coherent phase.
4. Steps 1–3 were repeated for  $D$ , yielding  $D_{\text{composite}} = |D_1|e^{i\angle D_2}$ .
5. Finally, the encoded slices were resolved using  $S_{\text{composite}}$  and  $D_{\text{composite}}$  images, and Eq. [4]. Note that, because all repetitions for  $S$  and  $D$  were acquired during the same time point in the cardiac cycle, both  $S$  and  $D$  are expected to have the same reproducible phase term. This shared phase term would not cause any interference between the resolved slices, as can be seen from Eq. [4].

This reconstruction scheme successfully resolves the Hadamard-encoded slices, as shown in the following section. For all EPI images, a reference scan correction was used to correct for the shifts between even/odd lines in k-space (34). A POCS algorithm was used for partial k-space reconstruction (35). After all the images were reconstructed, the ADC maps were generated for each resolved slice.

## RESULTS

### Simulation Results

The resulting Hadamard RF pulses  $\{RF_S, RF_D\}$  and the gradient pulses are shown in Figure 3a. The gray dashed and solid black lines represent the original and VERSE versions of the RF/gradient pulses, respectively. The pulse durations were reduced from 15.5 to 3.6 ms with the VERSE algorithm. This corresponds to more than 75% reduction in duration, which would result in about a 10% increase in white-matter SNR due to a shortened TE [assuming  $T_2 = 80$  ms for healthy white matter (36)].

While the shorter pulse durations come at the expense of increased gradient amplitude and RF power, the in vivo imaging sequence was still well within the SAR safety limits. We compared RF power depositions of a regular single-band  $180^\circ$  RF pulse (the initial single-band RF pulse of 7.8 ms duration described in the Methods section), the pre-VERSE Hadamard pulses (15.5 ms duration), and post-VERSE Hadamard pulses (3.6 ms duration). These RF pulses had the peak  $B_1$  constraint of 15  $\mu\text{T}$ . When compared to the single-band RF pulse, the pre-VERSE and post-VERSE Hadamard pulses had 2% and 50% higher RF power depositions, respectively. The reason that the pre-VERSE pulses had similar RF power deposition as the single-band pulse was the fact that they were stretched in time to meet the peak  $B_1$  limit. Their increased durations reduced their duty cycles and compensated for what would otherwise be an increased power deposition. For the post-VERSE Hadamard pulses, the increased power depositions were mostly due to the shortening in pulse durations. Similarly, the power deposition of the 2D-EPRF pulse (19.8 ms duration) was compared to that of a regular  $90^\circ$  RF pulse (1.5 ms). Due to its long duration, the 2D-EPRF pulse had approximately 17% reduced power deposition when compared to the regular  $90^\circ$  RF pulse. Overall, the “2D-EPRF - Hadamard” pulse pair had 32% increased power deposition per excitation when compared to a regular  $90^\circ$ – $180^\circ$  spin-echo pulse pair. With this modest increase in SAR, the proposed method achieves a 100% increase in slice coverage.

The simulated slice profiles for the  $RF_S$  and  $RF_D$  pulses, denoted as  $S$  and  $D$ , and the resolved slices,  $(S+D)/2$  and  $(S-D)/2$ , are given in Figure 3b,c. The maximum amplitude of interslice crosstalk is only 0.1%. This low crosstalk level is owing to the use of the SLR transform during the Hadamard pulse design.

Figure 4 demonstrates the effects of the delay between RF and gradient waveforms. For a timing error of 8  $\mu\text{s}$ , the Hadamard scheme exhibits an increased crosstalk level (Fig. 4a). Given in Figure 4b are the crosstalk levels between the bands for timing errors of  $-16$  to  $16$   $\mu\text{s}$ , simulated with a step size of 4  $\mu\text{s}$ . We can observe that the crosstalk level is minimal within this realistic delay range, e.g., 1% at  $-16$   $\mu\text{s}$  delay. Note that the crosstalk is asymmetric with respect to the timing error, because the VERSE RF and gradient pulses are not symmetric in time. The RF/gradient delay can be easily kept below 4  $\mu\text{s}$  with fine tuning, for which the crosstalk remains well below 0.3%.

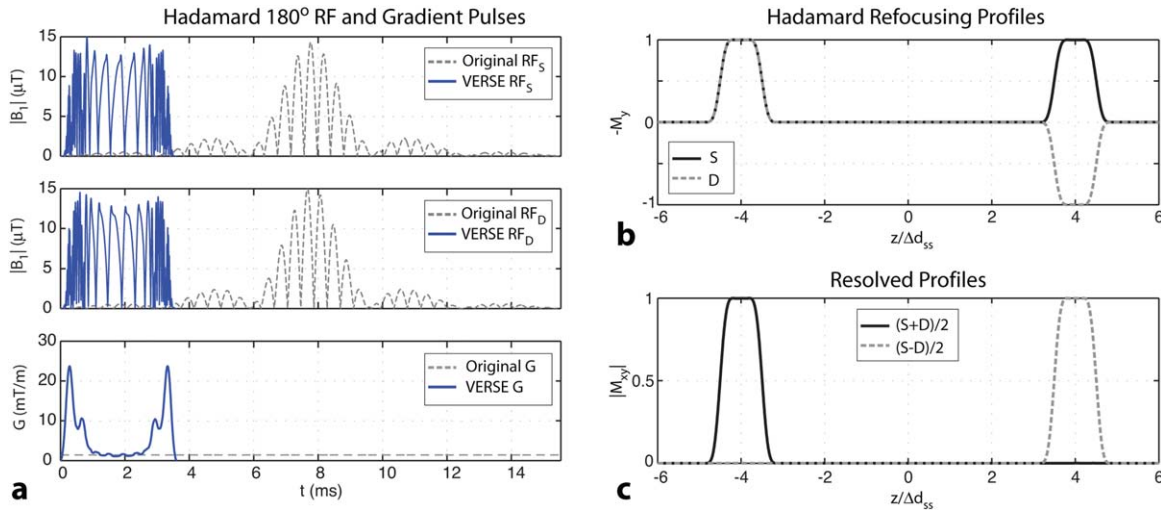


FIG. 3. The Hadamard RF and gradient pulses and the corresponding slice profiles. **a**: The original (i.e., pre-VERSE) and VERSE  $RF_S$  and  $RF_D$  pulses, along with the gradient waveform  $G$ . VERSE algorithm provides more than 75% reduction in pulse duration (from 15.5 to 3.6 ms). **b**: The simulated refocusing profiles provide an 8-slice separation between the two encoded slices.  $S$  and  $D$  denote the slice profiles for the  $RF_S$  and  $RF_D$  pulses, with **c**: the resolved slices  $(S+D)/2$  and  $(S-D)/2$  demonstrating minimal crosstalk. These profiles are simulated assuming a nonselective  $90^\circ$  excitation. [Color figure can be viewed in the online issue, which is available at [wileyonlinelibrary.com](http://wileyonlinelibrary.com).]

The sensitivity of the profiles to resonant offsets is presented in Figure 5. As seen in Figure 5a, the excitation profile of the 2D-EPRF pulse exhibits a large spatial shift in the slice direction due to its long duration. This shift is much smaller for the refocusing profiles of the Hadamard RF pulses, thanks to their shorter durations. However, due to the differences in spatial shifts, the excitation and refocusing profiles do not overlap entirely, which results in a partial refocusing of the excited slices. Figure 5b demonstrates that both resolved slices experience a small signal loss with increasing off-resonance, but are affected identically. Therefore, there is no signal mismatch between the resolved slices. At 64 Hz off-resonance, the signal level is at 75% when compared to the on-resonance signal level, i.e., there is a 25% signal loss. For reference, using a regular single-band  $180^\circ$  pulse with the same TBW and slice thickness would result in a 20% signal loss at 64 Hz off-resonance,

which is only slightly lower than that of the Hadamard pulse. As plotted in Figure 5c, a resonant offset also causes negligibly increased crosstalk between the resolved slices, e.g., 0.8% crosstalk at 64 Hz.

We also performed simulations to evaluate the sensitivity of the proposed method against  $B_1$  field inhomogeneities. The crosstalk remains below 1% for field variations of up to 30%. At 10% field variation, a maximum of 7% signal loss occurs, which is exactly the same as that of a regular single-band  $180^\circ$  pulse with the same TBW and slice thickness. Hence, the Hadamard RF pulses are as robust against  $B_1$  field inhomogeneities as any regular  $180^\circ$  pulse.

In conclusion, we deduce that the proposed Hadamard scheme exhibits minimal levels of crosstalk in the presence of timing errors, resonant offsets, and  $B_1$  field inhomogeneities. The signal loss due to off-resonance effects is comparable to that using a regular

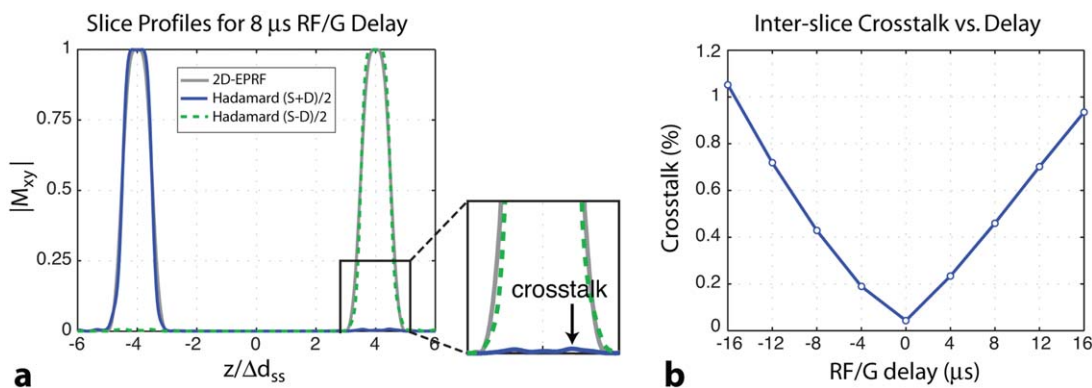


FIG. 4. The effects of RF/gradient timing errors. **a**: An 8 μs timing error causes an increased level of crosstalk between the resolved slices. **b**: The crosstalk maintains low levels, e.g., 1.05% at  $-16$  μs delay (plotted line represents crosstalk for both of the resolved slices). [Color figure can be viewed in the online issue, which is available at [wileyonlinelibrary.com](http://wileyonlinelibrary.com).]

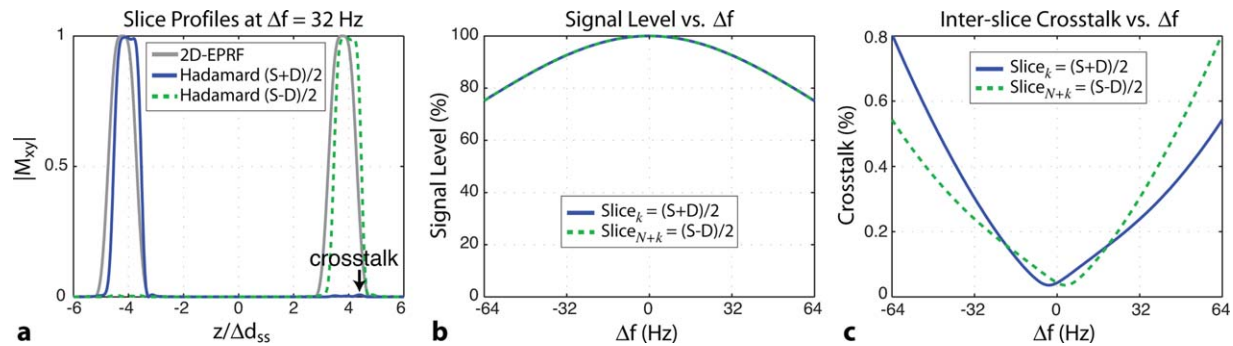


FIG. 5. The effects of resonant offsets on slice profiles. **a:** The excitation slice profile for the 2D-EPRF pulse experiences a larger spatial shift (in the  $-z$  direction) when compared to the refocusing profiles for the Hadamard RF pulses. The reduced overlap between the slice profiles result in a partial refocusing of the excited slice, which in turn leads to a decreased signal level. The resonant offset also causes increased crosstalk between the resolved slices, demonstrated here for a 32 Hz offset, corresponding to 0.5 ppm off-resonance at 1.5 T. **b:** The signal level slowly decreases as a function of increasing resonant offsets. At 64 Hz off-resonance (i.e., 1 ppm at 1.5 T), the signal level is at 75% (normalized by the signal level at on-resonance). Both resolved slices experience the same amount of signal decay, so there is no mismatch in the signal level. **c:** The crosstalk remains at minimal levels, e.g., 0.8% at 64 Hz. [Color figure can be viewed in the online issue, which is available at [wileyonlinelibrary.com](http://wileyonlinelibrary.com).]

180° pulse, and can be alleviated with proper shimming of the ROI. Similarly, the signal loss due to  $B_1$  field inhomogeneities is exactly the same as that using a regular 180° pulse.

#### Phantom Experiment Results

The measured slice profiles for the designed Hadamard pulses plotted in Figure 6a are in very good agreement with the simulated profiles. Note that the slice thicknesses for these pulses were 5 mm, corresponding to 40 mm separation between the two resolved slices. The measured crosstalk between the resolved slices was 1%, which falls within the range that was predicted by the simulation results for RF/gradient timing errors and resonant offsets given in Figures 4 and 5. Another contributing factor could be hardware imperfections such as eddy currents in the gradient coils.

The phantom experiment results given in Figure 6b validate the performance of the proposed scheme. Note that only two of the 16 resolved slices are shown, labeled as “slice 1” and “slice 9” as they are 8-slice apart. The physical distance between these two slices is 4 cm, and hence they capture completely different geometric features within the phantom. Identical display windowing was used in both images. These images clearly demonstrate that there is no visible interslice crosstalk, and the Hadamard scheme maintains the sharpness of the excitation profile in the PE direction (R/L in the image).

#### In Vivo Imaging Results

Figures 7 and 8 show the in vivo demonstration of the proposed Hadamard slice-encoding scheme with axial DWI of the spinal cord. The  $T_2$ -weighted (i.e.,  $b=0$ ) images and the isotropic diffusion-weighted ( $DW_{iso}$ ) images with  $b=500$  s/mm<sup>2</sup> are displayed. Figure 8 also displays the isotropic ADC maps ( $ADC_{iso}$ ) for all slices. The reduced-FOV was applied in the R/L direction,

which was the PE direction during the EPI readout. As seen in these figures, the reduced-FOV excitation in combination with the Hadamard encoding scheme is very effective in exciting only the ROI and enabling a high in-plane resolution of  $0.7 \times 0.7$  mm<sup>2</sup>.

Figure 7 shows both the Hadamard-encoded and resolved slices for two out of the 16 imaged slices. Here, the entire imaged FOV of  $9 \times 4.5$  cm<sup>2</sup> is displayed, and not a zoomed-in section. Because the Hadamard-encoded slices are 8-slice apart (i.e., the distance between two adjacent lobes of the 2D-EPRF pulse, equal to 4 cm for a slice thickness of 5 mm), they contain very different anatomical features. Nevertheless, there is no visible crosstalk between the resolved slices. Figure 8 shows  $4.5 \times 4.5$  cm<sup>2</sup> sections from all 16 slices of the in vivo imaging data set, demonstrating the reliability of the proposed scheme for the entire imaging volume. The ADC values were measured for all 16 slices in white matter ROIs. The mean values and standard deviations were  $ADC_{iso} = (916 \pm 156) \times 10^{-6}$  mm<sup>2</sup>/s for the isotropic ADC, and  $ADC_{SI} = (1840 \pm 233) \times 10^{-6}$  mm<sup>2</sup>/s for the S/I direction where the diffusivity is expected to be higher. Both of these values are in close proximity of those cited in the literature for healthy subjects (21).

#### DISCUSSION

The Hadamard slice-encoding scheme proposed in this work improves the reduced-FOV method in Ref. 5) by doubling the slice coverage, while preserving the original method's high-resolution imaging capabilities. The proposed modifications are along the slice-encoding direction only. Hence, a detailed analysis of the method was performed for robustness against potential problems such as interslice crosstalk and field-inhomogeneity induced signal loss. The image acquisition section, on the other hand, is not altered. Consequently, image quality is not expected to differ from what can be achieved using the original method in Ref. 5), where high-

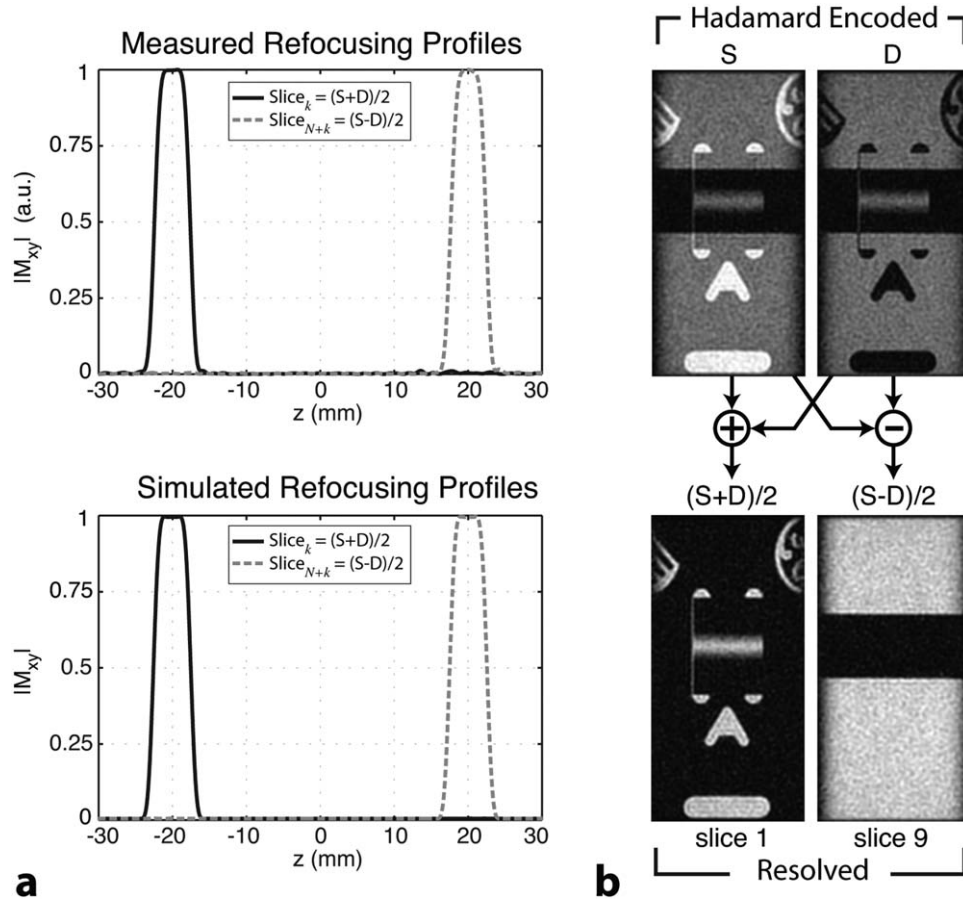


FIG. 6. Results of the phantom experiment for Hadamard slice-encoding scheme. **a**: Measured slice profiles for the resolved slices are in very good agreement with the simulated profiles. Note that the slice thickness for these pulses was 5 mm, with a 40 mm separation between the two slices. The measured crosstalk between the resolved slices is less than 1%. These profiles are measured/simulated using a nonselective  $90^\circ$  excitation. **b**: Phantom imaging results show no visible crosstalk between the resolved slices. Note that these two slices are 4-cm apart (i.e., the distance between two adjacent lobes of the 2D-EPRF pulse), and hence have completely different geometric features. The displayed images show the full imaging FOV of  $9 \times 4.5$  cm<sup>2</sup>, with  $0.7 \times 0.7$  mm<sup>2</sup> in-plane resolution and 5-mm slice thickness.  $\text{FOV}_{\text{PE}} = 4.5$  cm corresponds to the reduced-FOV direction (R/L in the image). As seen in these images, the Hadamard scheme does not hinder the performance of the reduced-FOV profile.

resolution in vivo images are achieved via a significant reduction in acquired k-space lines.

In theory, the proposed method doubles the slice coverage without any scan-time or SNR penalty. In practice, the SNR could be affected by the severity of the motion-induced phase or the number of NEXs acquired. Here, during the resolving of the Hadamard-encoded slices, we assumed that the motion-induced phase had two components: a reproducible phase term and a random phase noise. Previous work had shown that the motion-induced phase for brain DWI is fairly reproducible when cardiac gating is utilized (32). This also applies to spinal cord, as the cord was shown to move in an oscillatory pattern that is synchronized with the cardiac cycle (33). The phase noise, on the other hand, should increase with increased subject motion during diffusion-weighting gradients. Hence, the minimum number of averages required for the proposed phase estimation (i.e., Step 2 in Image Reconstruction) to work effectively depends on the extent of random motion. This argument follows directly from the law of large numbers. For the

healthy volunteer imaged in this work,  $\text{NEX} = 20$  averages per direction sufficed. A further evaluation in a clinical setting would be needed to determine if similar parameters can be used for clinical patients, who may exhibit increased involuntary motion.

In essence, all the reduced-FOV methods mentioned in the Introduction section serve to reduce distortions and enable high-resolution imaging with EPI (2–7). These methods are comparable in terms of their scan-time and high-resolution imaging capabilities, but may differ in terms of the effectiveness of their reduced-FOV profiles and slice coverages. When compared to other reduced-FOV methods, the proposed method offers multislice-imaging capability and the sharp 2D-EPRF excitation profile in the PE direction, so that no oversampling of the  $\text{FOV}_{\text{PE}}$  is needed. These are in contrast to the aforementioned ZOOM-EPI method that may require either a slice skip or an extended  $\text{FOV}_{\text{PE}}$  (2). Because only the ROI is excited, the proposed method is not prone to partial aliasing artifacts in the PE direction, unlike (3). A further advantage is the inherent fat suppression

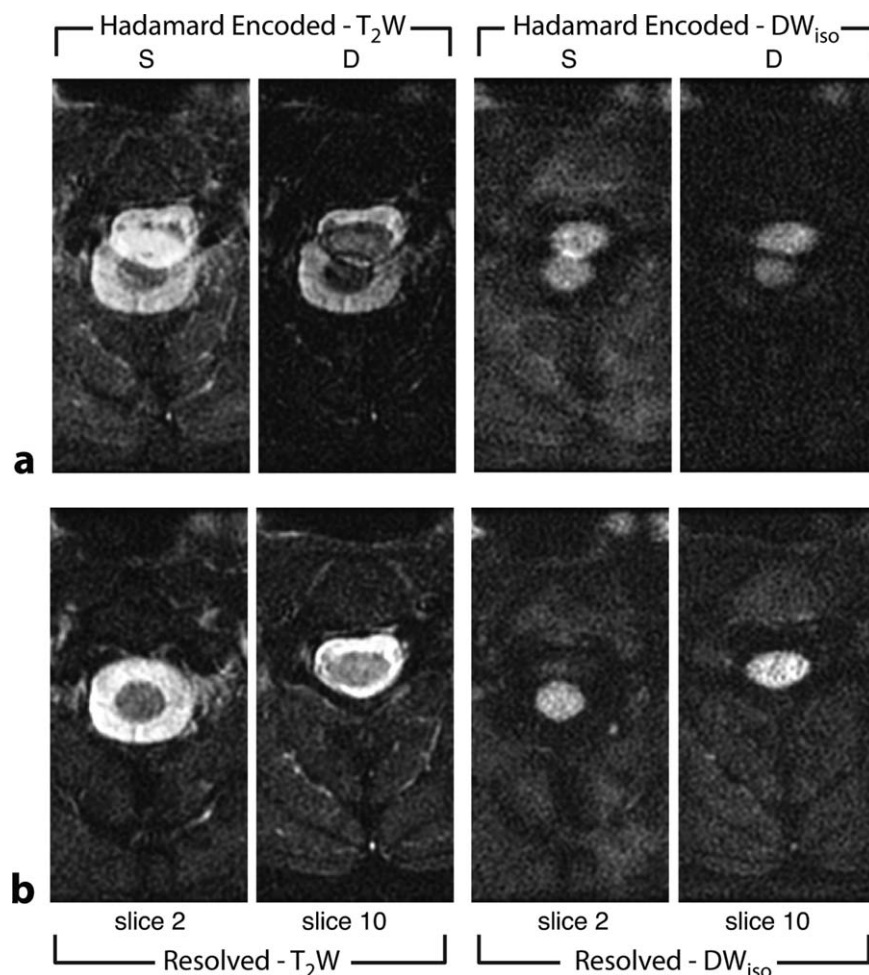


FIG. 7. In vivo demonstration of Hadamard slice-encoding scheme with axial DWI of the spinal cord. **a:** The encoded slices, *S* and *D*, have very different anatomical features, yet **b:** the resolved slices display no visible crosstalk. The  $T_2$ -weighted (i.e.,  $b=0$ ) images, and the isotropic diffusion-weighted ( $DW_{iso}$ ) images with  $b=500$  s/mm<sup>2</sup> are displayed. Only two out of the 16 imaged slices are displayed, and these two slices are 8-slice apart (i.e., the distance between two adjacent lobes of the 2D-EPRF pulse). The displayed images show the full imaging FOV of  $9 \times 4.5$  cm<sup>2</sup>, with  $0.7 \times 0.7$  mm<sup>2</sup> in-plane resolution and 5-mm slice thickness. The reduced-FOV was applied in the R/L direction, which was the PE direction during imaging. The images are windowed identically for each set.

capability of the 2D-EPRF pulse when followed by a 180° refocusing pulse.

#### Feasibility at Higher Fields

The in vivo imaging results in this work were performed at 1.5 T. As shown in our previous work on diffusion tensor imaging (DTI) of the spinal cord at 3 T (37), the 2D-EPRF excitation-based reduced-FOV method can produce high-quality DWI/DTI images at higher field strengths. Similarly, the proposed Hadamard-encoding scheme can also be applied successfully at higher fields. One potential drawback could be the off-resonance sensitivity of the method. As shown in Figure 5, a 64-Hz resonant offset causes approximately 25% signal loss. This offset is at a 1 ppm level at 1.5 T where our imaging experiments were performed, but corresponds to 0.5 ppm at 3 T. Hence, we expect the off-resonance sensitivity to be a bigger problem at higher fields. Note that this sensitivity stems from the long duration of the 2D-EPRF

pulse, and not the Hadamard RF pulses introduced in this work. Here, the RF deposition was also performed during the ramp up/down portions of the trapezoidal gradients, which helped reduce the total 2D-EPRF pulse length. More drastic shortenings in pulse duration can be achieved via an optimal VERSE design (17–19) where the plateaus of the gradients are also time optimized, or by utilizing parallel excitation schemes (38), or by combining both approaches (19,39). Shortening the 2D-EPRF pulse length would significantly alleviate the off-resonance sensitivity of this method.

#### Extending the Slice Coverage

The proposed Hadamard slice-encoding scheme successfully doubles the number of slices for a fixed scan time, by taking advantage of the periodic nature of the 2D-EPRF excitation profile. In vivo imaging results shown in this work feature sub-mm in-plane resolutions with relatively thick through-plane slices. These images were

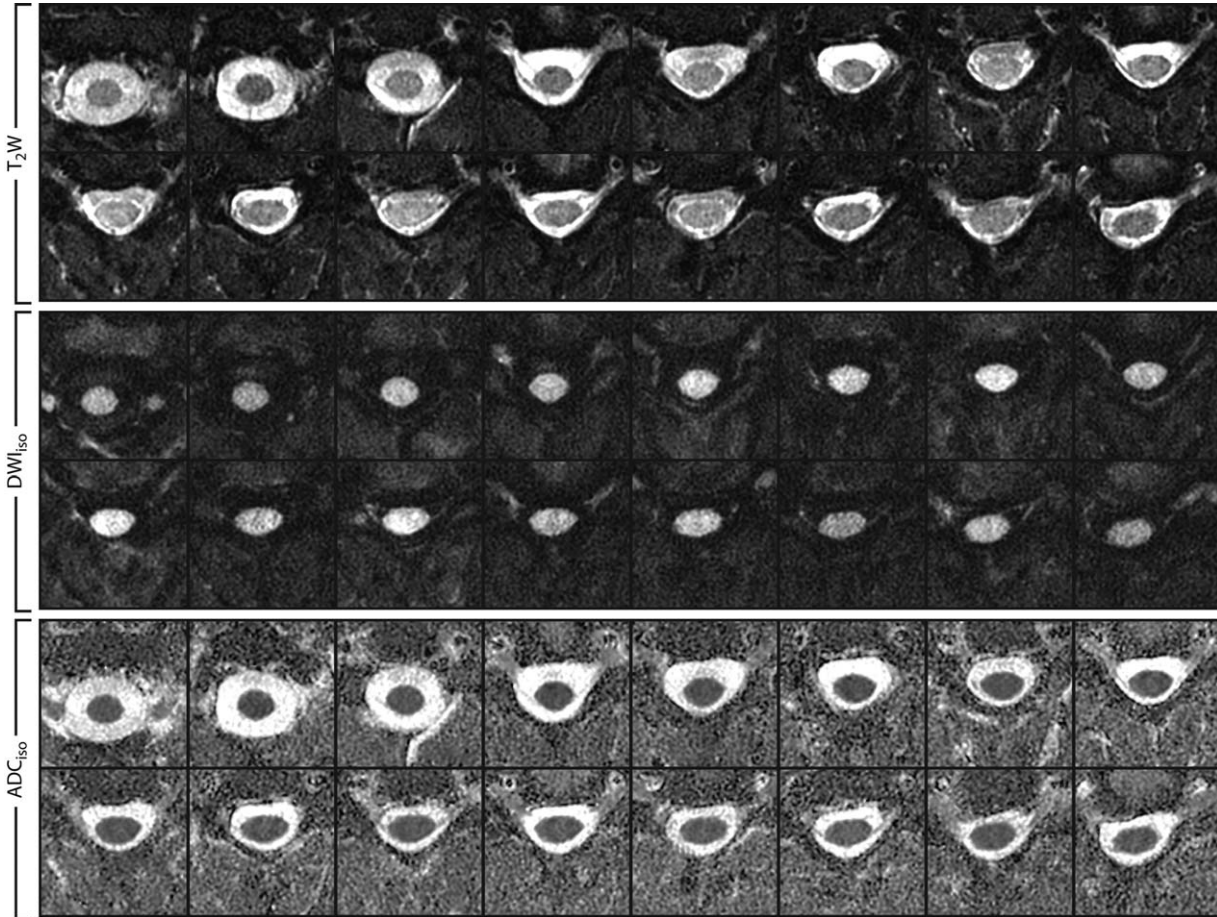


FIG. 8. All 16 slices from the in vivo demonstration of Hadamard slice-encoding scheme with axial DWI of the spinal cord. The  $T_2$ -weighted (i.e.,  $b = 0$ ) images, the isotropic diffusion-weighted ( $DWI_{iso}$ ) images with  $b = 500$  s/mm<sup>2</sup>, and the corresponding ADC maps are displayed. The displayed images show a central  $4.5 \times 4.5$  cm<sup>2</sup> section of the imaging FOV, with  $0.7 \times 0.7$  mm<sup>2</sup> in-plane resolution and 5-mm slice thickness.

acquired in the axial plane, which mostly coincided with the axial cross sections of the spinal cord. Because the spinal cord is only a couple of centimeters in diameter, the high in-plane resolution is crucial for resolving anatomical structures and potential pathology. Although the 5-mm slice thickness is not ideal, it helped to regain the SNR loss resulting from high in-plane resolution, as well as to increase the extent of coverage in the slice direction.

For DTI applications, isotropic resolution is usually desired to avoid bias during fiber tractography (40). With the proposed scheme, 1.4 mm isotropic resolution could be achieved while keeping the voxel size and the scan time the same as in Figure 7. However, the coverage in the slice direction would be significantly reduced due to the reduction in slice thickness. Hence, the proposed method may be more suited for applications where either thicker slices could be prescribed, or relatively small slice coverage suffices. For example, for spinal cord DTI applications, imaging could be performed in the sagittal plane, where the entire cord thickness can easily be covered with isotropic resolution. If there is a need to further extend the slice coverage, the proposed method can

be modified to include more lobes of the 2D excitation profile. For this purpose, Eq. [6] can be altered to achieve multiband refocusing of three or more lobes. The corresponding Hadamard RF pulses can then be shortened by using the methods described in this work.

The proposed method does not utilize parallel imaging to achieve multiband imaging capabilities, as opposed to the recently introduced multiband methods (41–45). However, parallel-imaging-based simultaneous multiband imaging could also be a potential extension of our method. Here, the periodic 2D-EPRF excitation profile would act as a multiband excitation, and a subsequent multiband refocusing pulse would select multiple side-lobes for simultaneous acquisition. These bands would then be resolved utilizing the known coil sensitivities. This technique would be similar in concept to the previous multiband imaging methods (41–45), with the added benefit of the reduced-FOV imaging capability. With this technique, there would not be a need to use a multiple-TR encoding/decoding scheme as done in this work. Hence, it may not require multiple NEXs and may be less sensitive to motion-induced phase issues. Feasibility of such a technique remains to be investigated.

## CONCLUSIONS

We have shown that Hadamard slice-encoding can successfully double the slice coverage for the 2D-EPRF reduced-FOV method, by taking advantage of the periodic excitation profile. This extension in slice coverage is achieved without any scan-time penalty, while preserving the inherent fat suppression capability of the original method. The SNR efficiency is improved by shortening the Hadamard RF pulses, while interleaved averaging and a phase-preserving reconstruction prevent interslice crosstalk. With phantom imaging experiments and *in vivo* axial DWI of the spinal cord, we demonstrated that the reduced-FOV excitation in combination with the Hadamard encoding scheme is very effective in achieving a high in-plane resolution with a wide coverage in the slice direction.

## ACKNOWLEDGMENTS

The authors thank Ehud Schmidt for the discussions on Hadamard encoding, and Jin Hyung Lee, Greg Zaharchuk, Nancy Fischbein, and Eric Han for their feedback and help throughout the study. This work was supported by Lucent Technologies Stanford Graduate Fellowship and GE Healthcare.

## REFERENCES

- Anderson AW, Gore JC. Analysis and correction of motion artifacts in diffusion weighted imaging. *Magn Reson Med* 1994;32:379–387.
- Wheeler-Kingshott CAM, Hickman SJ, Parker GJM, Ciccarelli O, Symms MR, Miller DH, Barker GJ. Investigating cervical spinal cord structure using axial diffusion tensor imaging. *Neuroimage* 2002;16:93–102.
- Wilm BJ, Svensson J, Hennig A, Pruessmann KP, Boesiger P, Kollias SS. Reduced field-of-view MRI using outer volume suppression for spinal cord diffusion imaging. *Magn Reson Med* 2007;57:625–630.
- Jeong EK, Kim SE, Guo J, Kholmovski EG, Parker DL. High-resolution DTI with 2D interleaved multislice reduced FOV single-shot diffusion-weighted EPI (2D ss-rFOV-DWEPI). *Magn Reson Med* 2005;54:1575–1579.
- Saritas EU, Cunningham CH, Lee JH, Han ET, Nishimura DG. DWI of the spinal cord with reduced FOV single-shot EPI. *Magn Reson Med* 2008;60:468–473.
- Finsterbusch J. High-resolution diffusion tensor imaging with inner field-of-view EPI. *J Magn Reson Imaging* 2009;29:987–993.
- Dowell NG, Jenkins TM, Ciccarelli O, Miller DH, Wheeler-Kingshott CAM. Contiguous-slice zonally oblique multislice (CO-ZOOM) diffusion tensor imaging: examples of *in vivo* spinal cord and optic nerve applications. *J Magn Reson Imaging* 2009;29:454–460.
- Zaharchuk G, Saritas EU, Andre JB, Chin CT, Rosenberg J, Brosnan TJ, Shankaranarayanan A, Nishimura DG, Fischbein NJ. Reduced field-of-view diffusion imaging of the human spinal cord: comparison with conventional single-shot echo-planar imaging. *Am J Neuroradiol* 2011;32:813–820.
- Andre JB, Saritas EU, Zaharchuk G, Rosenberg J, Komakula ST, Banerjee S, Shankaranarayanan A, Nishimura DG, Fischbein NJ. Clinical evaluation of reduced field-of-view diffusion-weighted imaging of the cervical and thoracic spine and spinal cord. *Am J Neuroradiol* 2012;33:1860–1866.
- Oh CH, Park HW, Cho ZH. Line-integral projection reconstruction (LPR) with slice encoding techniques: multislice regional imaging in NMR tomography. *IEEE Trans Med Imaging* 1984;3:170–178.
- Souza SP, Szumowski J, Dumoulin CL, Plewes DP, Glover G. SIMA: simultaneous multislice acquisition of MR images by Hadamard-encoded excitation. *J Comput Assist Tomogr* 1988;12:1026–1030.
- Yoo SS, Guttman CRG, Panych LP. Functional magnetic resonance imaging using non-Fourier, spatially selective radiofrequency encoding. *Magn Reson Med* 1999;41:759–766.
- Cunningham CH, Wood ML. Method for improved multiband excitation profiles using the Shinnar-Le Roux transform. *Magn Reson Med* 1999;42:577–584.
- Le Roux P. Exact synthesis of radio frequency waveforms. In *Proceedings of the 7th Annual Meeting of SMRM, San Francisco, 1988*. p. 1049.
- Shinnar M, Eleff S, Subramanian H, Leigh JS. The synthesis of pulse sequences yielding arbitrary magnetization vectors. *Magn Reson Med* 1989;12:74–80.
- Pauly J, Le Roux P, Nishimura D, Macovski A. Parameter relations for the Shinnar-Le Roux selective excitation pulse design algorithm. *IEEE Trans Med Imaging* 1991;10:53–65.
- Conolly S, Nishimura D, Macovski A, Glover G. Variable-rate selective excitation. *J Magn Reson* 1988;78:440–458.
- Hargreaves BA, Cunningham CH, Nishimura DG, Conolly SM. Variable-rate selective excitation for rapid MRI sequences. *Magn Reson Med* 2004;52:590–597.
- Lee D, Lustig M, Grissom WA, Pauly JM. Time-optimal design for multidimensional and parallel transmit variable-rate selective excitation. *Magn Reson Med* 2009;61:1471–1479.
- Eis M, Hoehn-Berlage M. Correction of gradient crosstalk and optimization of measurement parameters in diffusion MR imaging. *J Magn Reson B* 1995;107:222–234.
- Bammer R, Fazekas F. Diffusion imaging of the human spinal cord and the vertebral column. *Top Magn Reson Imaging* 2003;14:461–476.
- Cooke FJ, Blamire AM, Manners DN, Styles P, Rajagopalan B. Quantitative proton magnetic resonance spectroscopy of the cervical spinal cord. *Magn Reson Med* 2004;51:1122–1128.
- Poncellet BP, Wedeen VJ, Weisskoff RM, Cohen MS. Brain parenchyma motion: measurement with cine echo-planar MR imaging. *Radiology* 1992;185:645–651.
- Stejskal EO, Tanner JE. Spin diffusion measurements: spin echoes in the presence of a time-dependent field gradient. *J Chem Phys* 1965;42:288–292.
- Bammer R, Fazekas F, Augustin M, Simbrunner J, Strasser-Fuchs S, Seifert T, Stollberger R, Hartung HP. Diffusion-weighted MR imaging of the spinal cord. *Am J Neuroradiol* 2000;21:587–591.
- Clark CA, Werring DJ, Miller DH. Diffusion imaging of the spinal cord *in vivo*: estimation of the principal diffusivities and application to multiple sclerosis. *Magn Reson Med* 2000;43:133–138.
- Holder CA, Muthupillai R, Mukundan SJ, Eastwood JD, Hudgins PA. Diffusion-weighted MR imaging of the normal human spinal cord *in vivo*. *Am J Neuroradiol* 2000;21:1799–1806.
- Kuker W, Weller M, Klose U, Krapf H, Dichgans J, Nagele T. Diffusion-weighted MRI of spinal cord infarction: high resolution imaging and time course of diffusion abnormality. *J Neurol* 2004;251:818–824.
- Deo AA, Grill RJ, Hasan KM, Narayana PA. *In vivo* serial diffusion tensor imaging of experimental spinal cord injury. *J Neurosci Res* 2006;83:801–810.
- Saritas EU, Lee JH, Nishimura DG. SNR dependence of optimal parameters for apparent diffusion coefficient measurements. *IEEE Trans Med Imaging* 2011;30:424–437.
- Miller KL, Pauly JM. Nonlinear phase correction for navigated diffusion imaging. *Magn Reson Med* 2003;50:343–353.
- Nunes RG, Malik SJ, Hajnal JV. *In vivo* correction of non-linear phase patterns for diffusion-weighted FSE imaging using tailored RF excitation pulses. In *Proceedings of the 20th Annual Meeting of ISMRM, Melbourne, Australia, 2012*. p. 155.
- Mikulis DJ, Wood ML, Zerdoner OAM, Poncellet BP. Oscillatory motion of the normal cervical spinal cord. *Radiology* 1994;192:117–121.
- Bruder H, Fischer H, Reinfelder HE, Schmitt F. Image reconstruction for echo planar imaging with nonequidistant k-space sampling. *Magn Reson Med* 1992;23:311–323.
- Haacke EM, Lindscoj ED, Lin W. A fast, iterative, partial-fourier technique capable of local phase recovery. *J Magn Reson* 1991;92:126–145.
- Whittall KP, MacKay AL, Graeb DA, Nugent RA, Li DKB, Paty DW. *In vivo* measurement of T2 distributions and water content in normal human brain. *Magn Reson Med* 1997;37:34–43.
- Saritas EU, Zaharchuk G, Shankaranarayanan A, Aksoy M, Bammer R, Fischbein NJ, Boakye M, Nishimura DG. High-resolution DTI tractography of the spinal cord with reduced-FOV single-shot EPI at 3T. In *Proceedings of the 18th Annual Meeting of ISMRM, Stockholm, Sweden, 2010*. p. 3976.

38. Zhu Y. Parallel excitation with an array of transmit coils. *Magn Reson Med* 2004;51:775–784.
39. Lee D, Grissom WA, Kerr MLAB, Stang PP, Pauly JM. Verse-guided numerical RF pulse design: a fast method for peak RF power control. *Magn Reson Med* 2012;67:353–362.
40. Basser PJ, Pajevic S, Pierpaoli C, Duda J, Aldroubi A. In vivo fiber tractography using DT-MRI data. *Magn Reson Med* 2000;44:625–632.
41. Breuer FA, Blaimer M, Heidemann RM, Mueller MF, Griswold MA, Jakob PM. Controlled aliasing in parallel imaging results in higher acceleration (CAIPIRINHA) for multi-slice imaging. *Magn Reson Med* 2005;53:684–691.
42. Moeller S, Auerbach E, Van de Moortele P-F, Adriany G, Ugurbil K. fMRI with 16 fold reduction using multibanded multislice sampling. In: Proceedings of the 16th Annual Meeting of ISMRM, Toronto, Canada, 2008. p. 2366.
43. Moeller S, Yacoub E, Olman CA, Auerbach E, Strupp J, Harel N, Ugurbil K. Multiband multislice GE-EPI at 7 tesla, with 16-fold acceleration using partial parallel imaging with application to high spatial and temporal whole-brain fMRI. *Magn Reson Med* 2010;63:1144–1153.
44. Feinberg DA, Moeller S, Smith SM, Auerbach E, Ramanna S, Glasser MF, Miller KL, Ugurbil K, Yacoub E. Multiplexed echo planar imaging for sub-second whole brain fMRI and fast diffusion imaging. *PLoS One* 2010;5:e15710.
45. Setsompop K, Gagoski BA, Polimeni JR, Witzel T, Wedeen VJ, Wald LL. Blipped-controlled aliasing in parallel imaging for simultaneous multislice echo planar imaging with reduced g-factor penalty. *Magn Reson Med* 2012;67:1210–1224.